6380 *Inorg. Chem.* **2009**, *48*, 6380–6390
DOI: 10.1021/ic900628k

Inorganic Chemistry
Article

To What Extent Does the Zintl−Klemm Formalism Work? The $Eu(Zn_{1-x}Ge_x)_2$ Series

Tae-Soo You,[†] Sven Lidin,[‡] Olivier Gourdon,[§] Yaqiao Wu,[∥] and Gordon J. Miller*[,†]

[†]*Department of Chemistry, Iowa State University, Ames, Iowa 50011,* [‡]*Department of Physical, Inorganic and Structural Chemistry, Stockholm University, S-106 91 Stockholm, Sweden,* [§]*Jülich Center for Neutron Science — Neutron Scattering Science Division, Oak Ridge National Laboratory, Oak Ridge, Tennessee 37831-6032, and* [∥]*Ames Laboratory, U.S. Department of Energy, Iowa State University, Ames, Iowa 50011*

Received March 31, 2009

The series of ternary polar intermetallics $Eu(Zn_{1-x}Ge_x)_2$ ($0 \le x \le 1$) has been investigated and characterized by powder and single-crystal X-ray diffraction as well as physical property measurements. For $0.50(2) \le x < 0.75(2)$, this series shows a homogeneity width of hexagonal AlB_2-type phases (space group *P*6/*mmm*, Pearson symbol *hP*3) with Zn and Ge atoms statistically distributed in the planar polyanionic 6^3 nets. As the Ge content increases in this range, *a* decreases from 4.3631(6) Å to 4.2358(6) Å, while *c* increases from 4.3014(9) Å to 4.5759(9) Å, resulting in an increasing *c*/*a* ratio. Furthermore, the Zn−Ge bond distance in the hexagonal net drops from 2.5190(3) Å to 2.4455(3) Å, while the anisotropy of the displacement ellipsoids significantly increases along the *c* direction. For $x < 0.50$ and $x > 0.75$, respectively, orthorhombic KHg_2-type and trigonal $EuGe_2$-type phases occur as a second phase in mixtures with an AlB_2-type phase. Diffraction of the $x = 0.75(2)$ sample shows incommensurate modulation along the *c* direction; a structural model in super space group $P31(00\gamma)00s$ reveals puckered 6^3 nets. Temperature-dependent magnetic susceptibility measurements for two AlB_2-type compounds show Curie−Weiss behavior above 40.0(2) K and 45.5(2) K with magnetic moments of 7.98(1) μ_B for $Eu(Zn_{0.48}Ge_{0.52(2)})_2$ and 7.96(1) μ_B for $Eu(Zn_{0.30}Ge_{0.70(2)})_2$, respectively, indicating a $(4f)^7$ electronic configuration for Eu atoms (Eu^{2+}). The Zintl−Klemm formalism accounts for the lower limit of Ge content in the AlB_2-type phases but does not identify the observed upper limit. In a companion paper, the intrinsic relationships among chemical structures, compositions, and electronic structures are analyzed by electronic structure calculations.

Introduction

Polar intermetallic compounds represent a growing collection of inorganic solids used to investigate relationships among structures, physical properties, and chemical bonding.[1] They involve combinations of electropositive elements, that is, alkali- or alkaline-earth or rare-earth elements, with electronegative metals close to the Zintl line. The electronegative metals typically form networks that either conform to simple electron counting rules, such as the Zintl−Klemm formalism,[2−4] or give rise to an electronic structure characterized by a pseudogap in the electronic density of states curve and optimized orbital interactions at the Fermi level.[5] The electropositive metals formally act like cations, as in classical valence compounds (Zintl phases), by providing their valence electrons to influence the structure of the electronegative component. Their surroundings also involve large coordination numbers. However, unlike Zintl phases, these active metals do not transfer all valence electrons to the electronegative component but are involved in "lattice covalency" through their valence orbitals.[6] The presence of the pseudogap at the Fermi level can lead to potentially interesting physical properties, especially if rare-earth metals serve as the active metal due to partially filled 4f bands.[7] In general, polar intermetallics can be considered as a compound class intermediate between classical intermetallic compounds, such as Hume−Rothery electron phases, and Zintl−Klemm compounds.[2−4]

During our systematic investigation of the $Eu(M_{1-x}M'_x)_2$ series (M, M′ = group 12−14 elements) to study the correlation among atomic, electronic, and possible magnetic structures by varying atomic sizes and valence electron counts, we have observed a systematic structural variation within the $Eu(Zn_{1-x}Ge_x)_2$ system as *x* increases from the

*To whom correspondence should be addressed. E-mail: gmiller@iastate.edu.

(1) Westbrook, J. H.; Fleisher, R. L. *Intermetallic Compounds: Principle and Practices*; Wiley: New York, 1995.
(2) Nesper, R. *Prog. Solid State Chem.* **1990**, *20*, 1.
(3) Miller, G. J. In *Chemistry, Structure, and Bonding of Zintl Phases and Ions*; Kauzlarich, S. M., Ed.; VCH Publishers: New York, 1996; p 1.
(4) Schäfer, H. *Annu. Rev. Mater. Sci.* **1985**, *5*, 1.
(5) Miller, G. J.; Lee, C.-S.; Choe, W. In *Highlights in Inorganic Chemistry*; Meyer, G., Ed.; Wiley-VCH: Heidelberg, Germany, 2002; p 21.
(6) Klem, M. T.; Vaughy, J. T.; Harp, J. G.; Corbett, J. D. *Inorg. Chem.* **2001**, *40*, 7020.
(7) Gout, D.; Benbow, E.; Gourdon, O.; Miller, G. J. *J. Solid State Chem.* **2003**, *176*, 538.

 Published on Web 06/16/2009

KHg_2-type to the AlB_2-type and, finally, the $EuGe_2$-type structure. These structure types differ in the networks formed by the electronegative components: (a) the KHg_2-type shows a four-bonded, three-dimensional (4b-3D) net with locally distorted tetrahedral coordination; (b) the AlB_2-type contains three-bonded, two-dimensional (3b-2D) planes with trigonal-planar coordination; and (c) the $EuGe_2$-type exhibits 3b-2D puckered nets with local trigonal-pyramidal environments. The transition from planar to puckered three-connected nets has been discussed frequently in the literature[8] and is clearly related to the concentration of valence s and p electrons. In a recent study of EuGaTt (Tt = Si, Ge, Sn),[9] atomic size also influences puckering of 3b-2D nets, which is further mediated by the role of valence orbitals at the active metal site, that is, Eu, by creating multicentered interactions. In this paper, we have attempted to reduce the atomic size factor and to focus on valence electron count in the $Eu(Zn_{1-x}Ge_x)_2$ series. The $Eu(Zn_{1-x}Ge_x)_2$ compounds adopting the AlB_2-type phase are related to the superconducting AEAlSi (AE = Ca and Sr),[10−14] which have received recent attention for their similarity to superconducting MgB_2[15] with respect to their atomic structures and valence electron counts.

Experimental Section

Synthesis and Chemical Analysis. A total of 15 compositions along the $Eu(Zn_{1-x}Ge_x)_2$ series ($0 \le x \le 1$) were prepared using corresponding stoichiometric molar ratios of the pure elements (Eu: Ames Laboratory, 99.99%; Zn: Alfa, 99.999%; and Ge: Alfa, 99.999%) by induction-melting. Reactant mixtures were loaded into tantalum ampules, which were sealed by arc-melting in an argon-filled glovebox with a concentration of O_2 lower than 10 ppm. The tantalum ampules were then sealed in evacuated silica jackets to prevent oxidation. $EuZn_2$,[16] $Eu(Zn_{1-x}Ge_x)_2$, and $EuGe_2$[17] were heated, respectively, to 880, 1100, and 1050 °C and held at these temperatures for 15 min. Then, all products were allowed to cool to room temperature, and no subsequent annealing process was needed for any of the products, according to powder X-ray diffraction. All products remain visibly stable upon exposure to both air and moisture over several weeks. Analysis by energy-dispersive X-ray spectroscopy (EDXS) was conducted on a Hitachi S-2460N variable-pressure scanning electron microscope, equipped with an Oxford Instruments Link Isis Model 200 X-ray analyzer. The corresponding pure elements were used as standards for intensity references.

Crystal Structure Determination. The $Eu(Zn_{1-x}Ge_x)_2$ series was characterized at room temperature by both powder and single-crystal X-ray diffraction. Powder X-ray diffraction patterns were collected with a Huber G670 Guinier image-plate powder diffraction camera equipped with monochromatic Cu $K\alpha_1$ radiation ($\lambda = 1.54059$ Å). The step size was set at 0.005°, and the exposure time was 1−2 h. Data acquisition was controlled via the in situ program. The crystal systems and the lattice parameters were determined by Rietveld refinement using the program *Rietica*[18] and calibrated using Si powder (NIST, $a = 5.430940 \pm 0.000035$ Å) as a standard. These powder X-ray diffraction patterns were used to check the number and identity of phases in product mixtures, as well as to compare lattice parameters with subsequent single-crystal refinements. The two binary compounds, $EuZn_2$ and $EuGe_2$, as well as several multiphase products, were characterized solely by powder X-ray patterns. For the region below $x = 0.50(2)$, the hexagonal AlB_2-type phase coexisted with the orthorhombic phase $EuZn_2$. On the other hand, in the region of $x > 0.75(2)$, the trigonal phase $EuGe_2$ increasingly appeared as a secondary phase in product mixtures.

For single-crystal X-ray diffraction experiments of the AlB_2-type phases, several silvery lustrous crystals were selected from the cast of each product. The quality of each crystal was checked by a rapid scan on a Bruker SMART Apex CCD diffractometer with Mo Kα radiation ($\lambda = 0.71073$ Å). The best crystals were selected for further analysis, and then data were collected at 293(2) K using either a Bruker SMART Apex CCD diffractometer or a STOE IPDS diffractometer. On the Bruker SMART Apex CCD diffractometer, data were collected in a full sphere and harvested by taking three sets of 606 frames with 0.3° scans in ω and with an exposure time of 10 s per frame. On the STOE IPDS diffractometer, data from two sets of 180 frames were collected with an exposure time of 3 min for each frame. The angular range of 2θ was 9.0−70.0° for all compounds.

Intensities of the entire sets of reflections were extracted and corrected for Lorentz and polarization effects using the *SAINT* program,[19] and absorption was corrected empirically with the program *SADABS*.[19] The space group was determined by the program *XPREP* in the *SHELXTL* software package.[20] All structures were solved by direct methods and refined on F^2 by full-matrix least-squares methods using the *SHELXTL* software package.[20] The entire sets of reflections of $Eu(Zn_{1-x}Ge_x)_2$ for $0.50(2) \le x < 0.75(2)$ were matched with the hexagonal crystal system. Further analysis led us to choose $P6/mmm$ (AlB_2-type), in which Eu atoms are located at the origin (1*a* sites) of the hexagonal unit cells, and Zn and Ge atoms are statistically situated at $x = 1/3$, $y = 2/3$, and $z = 1/2$ (2d sites) with no preferred ordering.

Anisotropic displacement parameters of the Zn/Ge site along the *c* axis are larger than those along *a* and *b* axes in Ge-rich compositions of the AlB_2-type phases. This can indicate the tendency of puckering of anionic nets as previously observed by Pöttgen and Johrendt.[21] To check the possibility of puckering, space groups $P6_3mc$ and $P3m\bar{1}$ with a free atomic coordinate for the Zn/Ge atoms along the *c* axis were used for structural refinements. However, these refinements located the Zn/Ge atoms at $z = 0.4994(7)$. Moreover, an electron density contour map in the *ac* planes located at $x = 1/3$ and $x = 2/3$ showed just a single maximum at the Zn/Ge positions centered at $z = 1/2 \pm 0.0006(7)$ rather than two separated maxima. Therefore, $P6/mmm$ is chosen to be the most appropriate space group for structural refinement.

For $Eu(Zn_{0.25}Ge_{0.75(2)})_2$ specifically, which is the upper bound of the AlB_2-type phases, the diffraction pattern exhibits satellite reflections indicative of a uniaxial, incommensurate modulation along c^* with an incommensurate modulation vector $\mathbf{q} = (0, 0, 0.2200(1))$. The systematic absences are compatible with the super space group $P6/mmm(00\gamma)s00s$.

(8) Burdett, J. K.; Miller, G. J. *Chem. Mater.* **1990**, *2*, 12.
(9) You, T.-S.; Grin, Y.; Miller, G. J. *Inorg. Chem.* **2007**, *46*, 8801.
(10) Huang, G. Q.; Liu, M.; Chen, L. F.; Xing, D. Y. *Physica C* **2005**, *423*, 9.
(11) Imai, M.; Abe, E.; Ye, J.; Nishida, K.; Kimura, T.; Honma, K.; Abe, H; Kitazawa, H. *Phys. Rev. Lett.* **2001**, *87*, 077003.
(12) Imai, M.; Nishida, K.; Kimura, T.; Abe, H. *Appl. Phys. Lett.* **2002**, *80*, 1019.
(13) Imai, M.; Nishida, K.; Kimura, T.; Kitazawa, H.; Abe, H.; Kito, H.; Yoshii, K. *Physica C* **2002**, *382*, 361.
(14) Lorenz, B.; Lenzi, J.; Cmaidalka, J.; Meng, R. L.; Sun, Y. Y; Xue, Y. Y.; Chu, C. W. *Physica C* **2002**, *383*, 191.
(15) Nagamatsu, J.; Nakagawa, N.; Muranaka, T.; Zenitani, Y.; Akimitsu, J. *Nature* **2001**, *410*, 63.
(16) Iandelli, A.; Palenzona, A. *Atti Accad. Naz. Lincei Rend. Sci. Fis. Mat. Natur.* **1964**, *37*, 165.
(17) Hladyshevsky, E. I. *Dopov. Akad. Nauk.* **1964**, *2*, 209.
(18) Hunter, B. A.; Howard, C. J. *Rietica*; Australian Nuclear Science and Technology Organization: Menai, Australia, 2000.
(19) *XRD single crystal software*; Bruker Analytical X-ray System: Madison, WI, 2002.
(20) *SHELXTL*, version 5.1; Bruker AXS Inc.: Madison, WI, 1998.
(21) Pöttgen, R.; Johrendt, D. *Chem. Mater.* **2000**, *12*, 875.

The modulation was phased in two different ways: first, by simply taking the structural model for the three-dimensional basic structure as a starting point, allowing positional modulation of the Zn/Ge position, which immediately led to a drastic decrease in the R values for satellite reflections, and, second, by solving the structure ab initio using charge flipping[22] in super space[23] as implemented in the program *Superflip*.[24] Introducing second-order harmonics for the Zn/Ge position led to further improvement in the refinement, and the final agreement between model and data was satisfactory, $R_1 = 6\%$ for all main reflections and $R_1 = 22/30\%$ for observed/all satellite reflections. The relatively modest fit of the satellite reflections is easily understandable from their relative weakness. While 97% of the main satellites were ranked as observed above a $3\sigma(F)$ threshold, only 60% of the satellite reflections qualified according to that criterion. Due to the symmetry of the super space group and the special position of Eu, the amplitudes of all first-order modulations of this atom are identically zero. For second-order harmonics, a displacement along c is allowed, but this refined to a value far below the estimated standard deviation. In the final model, Eu was left as unaffected by the modulation.

If any symmetry lowering is to have some effect, it should allow for first-order harmonic modulations of the Eu position, which is at the origin. This is disallowed in $P6/mmm(00\gamma)s00s$ because of two distinct symmetry operations, namely, those given as boldface generators in $\boldsymbol{P6}/mmm(00\gamma)\boldsymbol{s}00s$ and $P6/mm\boldsymbol{m}(00\gamma)s00\boldsymbol{s}$. The first operation is a 6-fold rotation associated with a 1/2 phase shift in the internal parameter, that is, the symmetry operation $(x1\ x2\ x3\ x4) \rightarrow (x1-x2\ x1\ x3\ x4+1/2)$. The second operation is a reflection that exchanges $x2$ for $x3$, and this is also associated with a 1/2 phase shift of the internal parameter, that is, $(x1\ x2\ x3\ x4) \rightarrow (x1\ x3\ x2\ x4+1/2)$. When harmonic functions are used to describe the modulation, first-order harmonics at the origin are disallowed (see Appendix). Thus, all subgroups of $P6/mmm(00\gamma)s00s$ that retain either of these two operations will have the same symmetry constraint on first-order harmonics as does $P6/mmm(00\gamma)s00s$ itself and should be less interesting to consider.

The direct subgroups of $P6/mmm(00\gamma)s00s$ are $P6mm(00\gamma)s0s$, $P622(00\gamma)s00$, $P\bar{6}m2(00\gamma)000$, $P\bar{6}2m(00\gamma)00s$, $P6/m(00\gamma)s0$, $P\bar{3}m1(00\gamma)00s$, and $P\bar{3}m1(00\gamma)00s$. Among these, only $P6m2(00\gamma)000$ and $P\bar{3}m1(00\gamma)00s$ allow first-order harmonics for the modulation function of Eu along the z direction. When these two groups were tried, the centrosymmetric $P\bar{3}m1(00\gamma)00s$ required fewer parameters, but the z coordinate of the Zn/Ge site was variable, and led to a better R value. Therefore, this subgroup was deemed suitable for further investigations. As expected, the remaining five subgroups yielded models with inferior fits to the data.

The symmetry lowering also required introducing a twin law, defined in reciprocal space by the matrix

$$\begin{pmatrix} -1 & 0 & 0 \\ 0 & -1 & 0 \\ 0 & 0 & 1 \end{pmatrix}$$

that was used in this refinement. By adding successive displacive Fourier amplitude waves on the Zn/Ge atoms, as well as on the Eu atom, we slowly converged to a final solution with an overall R value around 6%. Analysis of the Zn/Ge site displacement showed the modulation curve has a "sawtooth"-like shape. Such behavior could be treated with a special function, such as a "sawtooth" function, or a combination of a Crenel (step) function of length $D = 1$ with the Legendre polynomials (note: the first-order Legendre polynomial is a linear function). By using the second approach, refinement converged to a final $R_1 = 5.38\%$ for all main reflections and $R_1 = 6.33/9.72\%$ for observed/all satellite reflections. The refined twin fraction is relatively close to 50% (for additional information, please see the Supporting Information, Table S3).

All refinements were performed using the *JANA2006*[25] software. Throughout all refinements, Zn and Ge cannot be unequivocally differentiated given their similar scattering factors in the X-ray diffraction experiment. Therefore, we assumed Zn and Ge atoms to be statistically distributed within the hexagonal nets according to the stoichiometric ratio provided by EDXS analyses during the refinement processes; however, neutron scattering experiments are underway to elucidate any possible modulation on the Zn/Ge occupation. Indeed, we suspect that the Ge and Zn atoms are not entirely statistically distributed, and that the displacive and occupancy modulations are somewhat related, which is undergoing further study.

Electron Microscopy. A Tecnai G2 F20 analytical scanning transmission electron microscope was employed for transmission electron microscopy (TEM)/high-resolution TEM (HRTEM) investigations on the $Eu(Zn_{0.25(2)}Ge_{0.75(2)})_2$ sample to probe possible superstructures of the AlB_2-type lattice. The TEM was operated at 200 kV for microstructure characterization. TEM samples were prepared by using the crush-and-float method.[26] Small pieces of alloys were crushed in a methanol solution using a mortar and a pestle and then dropped onto a carbon-coated 3-mm Cu grid with a lacey network support film from Ted Pella, Inc. The lacey support film contains holes varying in size from less than 0.25 μm to more than 10 μm, which is ideal for the specimens since the sizes of the crushed sample vary in the same range. The edges of the crushed small sample pieces can be as thin as 50 nm, which is ideal for TEM/HRTEM characterization.

Physical Property Measurements. Temperature-dependent magnetic susceptibility measurements for two compounds, $Eu(Zn_{0.48}Ge_{0.52(2)})_2$ and $Eu(Zn_{0.30}Ge_{0.70(2)})_2$, were conducted using a Quantum Design MPMS-5 SQUID magnetometer. The measured temperature range was 1.8−300 K with a magnetic field of 0.1 T. Magnetic measurements were carried out on bulk samples (approximately 300 mg) from the same preparations as the one used for powder diffraction experiments.

Temperature-dependent electrical resistivities of $Eu(Zn_{0.45}Ge_{0.55(2)})_2$ and $Eu(Zn_{0.33}Ge_{0.67(2)})_2$ were measured by the electrode-less "Q" method with the aid of a Hewlett-Packard 4342A Q-meter.[27] Approximately 110 mg of each sample ground with a grain diameter between 180 and 200 μm was mixed with chromatographic alumina and sealed into a Pyrex tube. The measurement was conducted at 34 MHz over the temperature range of ca. 110−230 K.

Results and Discussion

Five distinct regions of phase behavior were observed along the series $Eu(Zn_{1-x}Ge_x)_2$ according to X-ray powder diffraction, shown in Figure 1. Three of these regions show single-phase behavior, while the other two regions exhibit two-phase features: (1) $x = 0$ in Figure 1a, that is, $EuZn_2$, adopts the orthorhombic KHg_2 structure type; (2) $0 < x < 0.50(2)$ patterns, as in Figure 1b, contain orthorhombic KHg_2-type and hexagonal AlB_2-type characteristics; (3) $0.50(2) \leq x < 0.75(2)$ in Figure 1c and d is a single-phase region with patterns matching the AlB_2 structure type; (4)

(22) Oszlanyi, G.; Suto, A. *Acta Crystallogr.* **2004**, *A60*, 134.
(23) Palatinus, L. *Acta Crystallogr.* **2004**, *A60*, 604.
(24) Palatinus, L.; Chapuis, G. *J. Appl. Crystallogr.* **2007**, *40*, 786.
(25) Petricek,V.; Dusek, M.; Palatinus, L. *Jana2006*; The Crystallographic Computing System, Institute of Physics: Praha, Czech Republic, 2006.
(26) Williams, B. D.; Carter, B.; *Transmission Electron Spectroscopy*; Plenum Press: London, 1996.
(27) Zhao, J. T.; Corbett, J. D. *Inorg. Chem.* **1995**, *34*, 378.

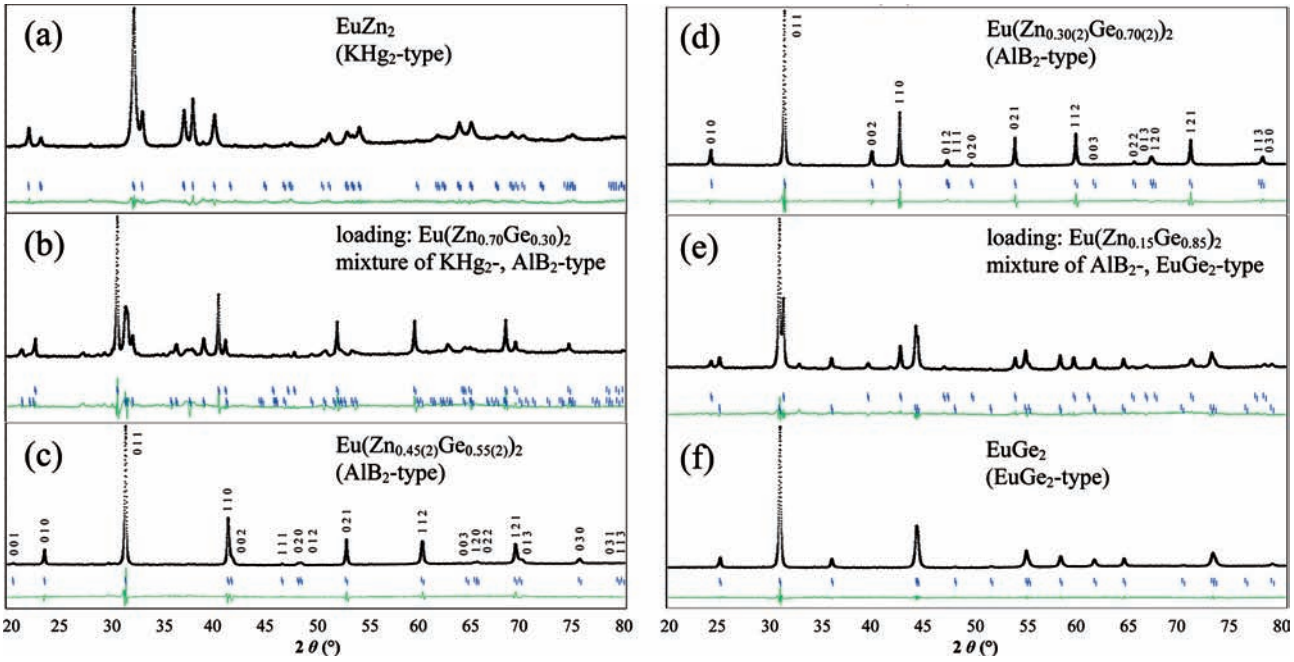

Figure 1. Powder X-ray diffraction patterns of selected samples from the $Eu(Zn_{1-x}Ge_x)_2$ series ($0 \le x \le 1$). Miller indices are also shown for two AlB_2-type phases (c and d).

Table 1. Lattice Constants and Unit Cell Volumes As Determined by X-Ray Powder Diffraction for $Eu(Zn_{1-x}Ge_x)_2$ ($0 \le x \le 1$)[a]

x (loaded)	*x* (EDXS)	structure type	*a* (Å)	*b* (Å)	*c* (Å)	(*c*/*a*)* (Å)	*V** (Å^3)
0.00	0.00(2)	KHg_2	4.7313(6)	7.6444(9)	7.6564(9)	0.808	69.23(2)
0.17		KHg_2	4.6964(3)	7.6249(5)	7.7269(6)	0.812	69.18(1)
	0.49(2)	AlB_2	4.3692(2)	4.3692(2)	4.3000(2)	0.985	71.09(1)
0.30		KHg_2	4.6770(2)	7.6346(4)	7.7604(4)	0.816	69.28(1)
	0.50(2)	AlB_2	4.3670(2)	4.3670(2)	4.3098(1)	0.987	71.18(1)
0.40		KHg_2	4.6617(5)	7.6283(8)	7.7830(1)	0.818	69.19(2)
	0.50(2)	AlB_2	4.3668(1)	4.3668(1)	4.3187(1)	0.989	71.32(1)
0.45		KHg_2	4.6443(1)	7.5996(1)	7.7438(1)	0.818	68.33(1)
	0.50(2)	AlB_2	4.3549(3)	4.3549(3)	4.2998(3)	0.987	70.62(1)
0.50	0.52(2)	AlB_2	4.3577(2)	4.3577(2)	4.3239(1)	0.992	71.11(1)
0.55	0.55(2)	AlB_2	4.3137(2)	4.3137(2)	4.4036(2)	1.021	70.96(1)
0.60	0.60(2)	AlB_2	4.3035(1)	4.3035(1)	4.4584(2)	1.036	71.51(1)
0.65	0.67(2)	AlB_2	4.2581(3)	4.2581(3)	4.5221(5)	1.062	71.01(1)
0.69	0.70(2)	AlB_2	4.2558(1)	4.2558(1)	4.5321(1)	1.065	71.09(1)
0.73	0.75(2)	AlB_2	4.2546(2)	4.2546(2)	4.5623(2)	1.072	71.52(1)
0.78	0.76(2)	AlB_2	4.2346(1)	4.2346(1)	4.5728(1)	1.080	71.01(1)
		$EuGe_2$	4.1040(1)	4.1040(1)	4.9983(1)	1.218	72.91(3)
0.80	0.76(2)	AlB_2	4.2349(4)	4.2349(4)	4.5733(5)	1.080	71.03(1)
		$EuGe_2$	4.1045(2)	4.1045(2)	4.9950(1)	1.217	72.88(1)
0.85	0.75(2)	AlB_2	4.2448(1)	4.2448(1)	4.5656(2)	1.076	71.24(1)
		$EuGe_2$	4.1075(1)	4.1075(1)	4.9974(2)	1.217	73.02(1)
1.00	1.00(2)	$EuGe_2$	4.1044(4)	4.1044(4)	4.9996(1)	1.218	72.94(1)

[a] *V** = volume per formula unit; (*c*/*a*)* = *c*/*a* for hexagonal AlB_2-type and = *b*/2*a* for orthorhombic KHg_2-type samples.

$0.75(2) < x < 1$ patterns, as in Figure 1e, have hexagonal AlB_2-type and trigonal $EuGe_2$-type features; and (5) $x = 1$ in Figure 1f, that is, $EuGe_2$, forms the trigonal $EuGe_2$ structure type. All Rietveld refinements of powder diffraction patterns produced lattice parameters in very good agreement with those obtained from single-crystal X-ray diffraction experiments throughout the entire series, as listed in Table 1. The crystallographic results of four distinct single-crystal specimens adopting the AlB_2-type structure are summarized in Table 2.

Regions 1 and 2: $Eu(Zn_{1-x}Ge_x)_2$. The KHg_2-type structure (space group *Imma*) of $EuZn_2$, shown in Figure 2 (left),[16] is closely related to the hexagonal AlB_2-type because both structures contain 6^3 anionic nets stacked in an eclipsed manner with larger atoms located between them.[28] The hexagonal nets in $EuZn_2$ are puckered in a manner to create Zn−Zn contacts between nets and a distorted tetrahedral environment at each Zn atom. This puckering is expected on the basis of how closely these sheets approach each other along the stacking direction, that is, the *b* axis, an approach which can be measured by the *b*/2*a* ratio (these fall under the (*c*/*a*)* column in Table 1 as an analogy to the *c*/*a* ratios for the hexagonal and trigonal phases).[8] The Zn−Zn distances between adjacent

(28) Pöttgen, R.; Kotzyba, G.; Schappacher, F. M.; Mosel, B. D.; Eckert, H.; Grin, Y. *Z. Anorg. Allg. Chem.* **2001**, *627*, 1299.

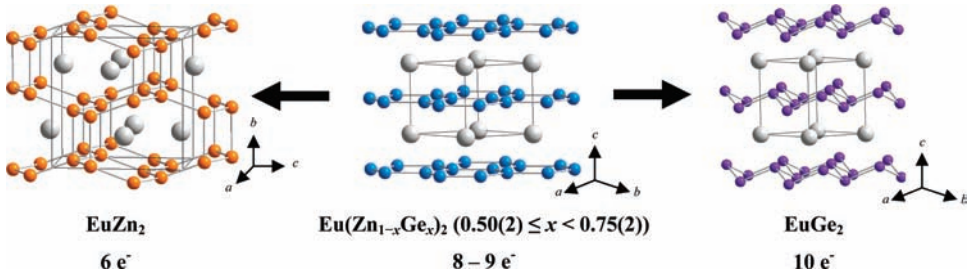

Figure 2. Crystal structures of $EuZn_2$ (KHg_2-type), $Eu(Zn_{1-x}Ge_x)_2$ ($0.50(2) \le x < 0.75(2)$, AlB_2-type) and $EuGe_2$ ($EuGe_2$-type) with valence electron counts. Eu, gray; Zn, orange; Zn/Ge, blue; Ge, purple.

Table 2. Crystallographic Data for $Eu(Zn_{1-x}Ge_x)_2$ (x = 0.50(2), 0.55(2), 0.67(2), 0.70(2))

		$Eu(Zn_{0.50(2)}Ge_{0.50(2)})_2$	$Eu(Zn_{0.45(2)}Ge_{0.55(2)})_2$	$Eu(Zn_{0.33(2)}Ge_{0.67(2)})_2$	$Eu(Zn_{0.30(2)}Ge_{0.70(2)})_2$
fw (g mol^{-1})		289.96	290.68	292.41	293.57
unit cell parameters (Å)		a = 4.3577(2)	a = 4.3137(2)	a = 4.2581(3)	a = 4.2558(1)
		c = 4.3239(1)	c = 4.4036(2)	c = 4.5221(5)	c = 4.5321(1)
V (Å^3)		71.11(1)	70.96(1)	71.01(1)	71.09(1)
density, calcd. (g cm^{-3})		6.77	6.80	6.84	6.86
diffractometer		STOE IPDS	SMART Apex	SMART Apex	AMART Apex
index ranges		$-6 \le h \le 6$	$-6 \le h \le 6$	$-6 \le h \le 6$	$-6 \le h \le 6$
		$-6 \le k \le -7$	$-6 \le k \le -6$	$-6 \le k \le 6$	$-6 \le k \le 6$
		$-6 \le l \le 6$	$-7 \le l \le 7$	$-7 \le l \le 7$	$-7 \le l \le 7$
no. reflns		1296	1052	1033	1037
independent reflns		87 [R_{init} = 0.0550]	88 [R_{init} = 0.0325]	87 [R_{init} = 0.0312]	89 [R_{init} = 0.0355]
data/params		87/6	88/5	86/6	89/6
GOF on F^2		1.231	1.067	1.204	1.219
R indices [$I > 2\sigma(I)$]		$R1$ = 0.0344	$R1$ = 0.0154	$R1$ = 0.0131	$R1$ = 0.0109
		$wR2$ = 0.0769	$wR2$ = 0.0321	$wR2$ = 0.0305	$wR2$ = 0.0248
R indices (all data)		$R1$ = 0.0427	$R1$ = 0.0164	$R1$ = 0.0131	$R1$ = 0.0109
		$wR2$ = 0.0791	$wR2$ = 0.0325	$wR2$ = 0.0305	$wR2$ = 0.0248
diff. peak and hole (e$^-$/Å^3)		1.724/−2.549	1.490/−0.648	1.106/−0.641	1.335/−0.603
U_{eq}	Eu (1*a*)	0.013(1)	0.010(1)	0.011(1)	0.011(1)
	Zn/Ge (2*d*)	0.014(1)	0.014(1)	0.021(1)	0.027(1)
U_{33}/U_{11}	Eu (1*a*)	1.00	1.33	1.00	1.00
	Zn/Ge (2*d*)	1.91	3.38	4.89	7.11

distorted 6^3 nets (parallel to the b axis) are ca. 7% longer than those within the net. These distortions produce zigzag ribbons of rectangles formed by Zn atoms along the a axis. The Eu atoms are symmetrically displaced along the c axis away from these networks.

A KHg_2-type phase also occurs in each powder pattern of $Eu(Zn_{1-x}Ge_x)_2$ samples for $x < 0.50(2)$. Refinements of lattice constants suggest that Ge atoms replace a small number of Zn atoms, but we have no further chemical analysis of these phases and have not identified the upper bound of the single-phase KHg_2-type $Eu(Zn_{1-x}Ge_x)_2$ region. Analysis of the theoretical electronic structure of $EuZn_2$ also suggests that the orthorhombic KHg_2 structure type is a stable structure for Ge substitution for a small number of Zn atoms.[29]

Region 3: $EuZn_{1-y}Ge_{1+y}$. As the amount of Ge increases in $Eu(Zn_{1-x}Ge_x)_2$, the AlB_2-type phase emerges in product mixtures, as shown in Figure 1b, and becomes single-phase when x reaches 0.50(2). This region remains single-phase up to $x < 0.75(2)$, as seen in Figure 1c and d, indicating a wide homogeneity range for this phase. Given this observation, we reformulate these ternary phases as $EuZn_{1-y}Ge_{1+y}$ ($0 \le y \le 0.50(2)$).

According to Figure 3, the lattice parameters, a and c, show opposite trends with increasing Ge content in these $EuZn_{1-y}Ge_{1+y}$ phases: the a axis decreases by ca. 2.6% while the c axis increases by ca. 5.3% from $y = 0$ ($EuZn_{1.00}Ge_{1.00(2)}$) to $y = 0.40$ ($EuZn_{0.60}Ge_{1.40(2)}$). These trends suggest increasing attractive interactions, possibly via π overlap, within the 6^3 nets, while the interlayer forces become increasingly repulsive. Moreover, the c/a ratios as well as the unit cell volumes (not shown) strictly increase with Ge content. It is also notable that $c/a > 1$ for the lower Ge contents, that is, for $y \le 0.04$, and $c/a > 1$ for higher Ge contents, that is, for $y \ge 0.10$.

The crystal structures of these ternary compounds contain $^2_\infty[(Zn_{1-y}Ge_{1+y})_2]$ planar 6^3 nets (Figure 2, middle) with Eu atoms occupying the hexagonal prismatic voids. The observed Zn/Ge−Zn/Ge distances within the 6^3 nets range from 2.5190(3) Å for $Eu(Zn_{0.50}Ge_{0.50(2)})_2$ to 2.4545 (2) Å for $Eu(Zn_{0.30}Ge_{0.70(2)})_2$, distances which are significantly shorter than the range of the sums of 12-coordinate, metallic radii of Zn and Ge (2.756−2.788 Å: r(Zn) = 1.394 Å, r(Ge) = 1.378 Å[30]) but are in excellent agreement with the sums of their covalent radii (2.44−2.50 Å: r(Zn) = 1.25 Å, r(Ge) = 1.22 Å[31]). We should note that the average Zn−Zn and Ge−Ge distances in $EuZn_2$ (2.699 Å)[16] and $EuGe_2$ (2.564(4) Å)[32] lie between the corresponding sums of metallic and covalent radii. In $EuZn_{1-y}Ge_{1+y}$,

(29) You, T.-S.; Miller, G. J. *Inorg. Chem.* **2009** companion article following.

(30) Teatum, E.; Gshneidner, K., Jr.; Waber, J. *Radii of the Elements for CN12*; U.S. Department of Commerce: Washington, DC, 1960; LA-2345.

(31) Emsley, J. *The Elements*; Clarendon Press: Oxford, U.K., 1998.

(32) Bobev, S.; Bauer, E. D.; Thompson, J. D.; Sarrao, J. L.; Miller, G. J.; Eck, B.; Dronskowski, R. *J. Solid State Chem.* **2004**, *177*, 3545–3552.

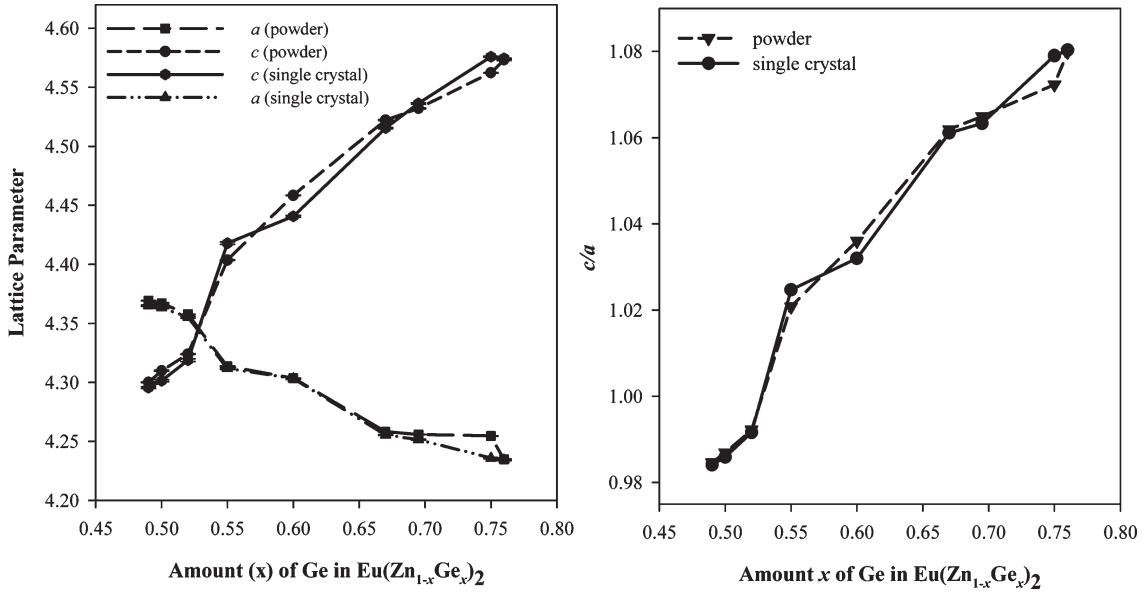

Figure 3. (Left) Lattice parameters a and c (left), c/a ratio (right), the number of valence electrons, and Zn−Ge bond distances of the AlB_2-type phase of $Eu(Zn_{1-x}Ge_x)_2$ series as a function of the amount of Ge.

therefore, the observed Zn/Ge−Zn/Ge distances indicate strong polar covalent interactions within the polyanionic nets, which will be further influenced by electron transfer from the electropositive Eu atoms to the electronegative Zn and Ge atoms. Aspects of the chemical bonding in these compounds have been analyzed using electronic structure calculations, which can also account for the observed upper limit in Ge content in this homologous series and will be discussed in a companion article.[29]

The temperature-dependent magnetic susceptibilities of two limiting compositions, $Eu(Zn_{0.48(2)}Ge_{0.52(2)})_2$ and $Eu(Zn_{0.30(2)}Ge_{0.70(2)})_2$, are dominated by the magnetic moment of Eu atoms and show essentially Curie−Weiss behavior in corresponding paramagnetic regions with either ferromagnetic (FM) or antiferromagnetic (AFM) behavior at low temperatures (see the Supporting Information). Effective magnetic moments for each compound, as calculated from the corresponding slopes of the $1/\chi$ versus T plots and corrected for the temperature-independent terms, gave 7.98(1) μ_B for $Eu(Zn_{0.48(2)}Ge_{0.52(2)})_2$ and 7.96(1) μ_B for $Eu(Zn_{0.30(2)}Ge_{0.70(2)})_2$, both of which are very close to the value of the Eu^{2+} free ion, 7.94 μ_B, to indicate a $(4f)^7$ electronic configuration for Eu. $Eu(Zn_{0.48(2)}Ge_{0.52(2)})_2$ shows Curie−Weiss behavior at temperatures above 40.0(2) K, while below this temperature the susceptibility becomes dependent on the external magnetic field, resulting in FM ordering with $\theta_p = +15.3$ (3) K. On the other hand, $Eu(Zn_{0.30(2)}Ge_{0.70(2)})_2$ displays Curie−Weiss paramagnetism above 45.0(2) K and shows AFM ordering with $\theta_p = -1.95(3)$ K. Furthermore, the extrapolation of measured resistivities shows room-temperature values of ca. 1.40×10^{-5} and 2.08×10^{-5} Ω m, respectively, for $Eu(Zn_{0.45(2)}Ge_{0.55(2)})_2$ and $Eu(Zn_{0.33(2)}Ge_{0.67(2)})_2$, that decrease linearly over a temperature range from ca. 110−230 K, features which are indicative of either semiconducting or semimetallic behavior of these samples (see the Supporting Information).

An additional significant result observed from the single-crystal diffraction results of the $EuZn_{1-y}Ge_{1+y}$ phases is the substantial increase of U_{33}/U_{11} ratios at the Zn/Ge (2d) sites as the Ge content increases, see Table 1, from 1.91 in $EuZn_{1.00(2)}Ge_{1.00(2)}$ to 7.11 in $EuZn_{0.60(2)}Ge_{1.40(2)}$. As we mentioned earlier, all refinement attempts converge toward planar $^2_\infty[(Zn_{1-y}Ge_{1+y})_2]$ 6^3 nets, even when space groups are selected that allow the z coordinate of the 2d sites to be free parameters. Nevertheless, the tendency to pucker the 6^3 nets increases steadily and significantly as the Ge content increases. Similar behavior is observed in $Eu(Ga_{1-x}Si_x)_2$, which adopts the AlB_2-type for $0.19(2) \leq x \leq 0.76(2)$ and also shows an increasing tendency toward puckering of the 6^3 nets as the Si content increases according to U_{33}/U_{11} ratios.[33] Moreover, $Eu(Ga_{1-x}Ge_x)_2$ exhibits observable puckering in its structures for $x \geq 0.50$.[33]

The most Ge-rich phase we studied by diffraction methods, $Eu(Zn_{0.25}Ge_{0.75(2)})_2$, yielded incommensurately modulated diffraction peaks from both single-crystal X-ray diffraction as well as from HRTEM (see Figure 4). In this incommensurately modulated structure, the superstructure is driven probably by the tendency to pucker the 6^3 nets coupled with the distribution of Zn and Ge atoms in each net. Due to the symmetry constraints on the Zn/Ge position, displacement is only allowed along the c axis, and this motion may be modeled in two different ways. In our first model with super space group $P6/mmm(00\gamma)$-$s00s$, shown in Figure 5 (left), the modulation is treated as a sum of two harmonic displacements. This model yielded a satisfactory fit to the data, but its three-dimensional interpretation is one where the puckering of the Zn/Ge nets varies continuously from layer to layer. Distances within the 6^3 nets range from 2.464 to 2.521 Å, and the puckering, as gauged by the "thickness" of the puckered net, varies from 0.352 to 0.632 Å with an average value of 0.516 Å (note: for a planar net, the "thickness" would be 0 Å). In a second model shown in Figure 5 (right), the displacement of the Zn/Ge site was modeled primarily by a sawtooth displacement with an additional second-order

(33) You, T.-S.; Zhao, J.-T.; Pöttgen, R.; Schnelle, W.; Burkhardt, U.; Grin, Y.; Miller, G. J. *Chem. Mater.* **2009**, submitted for publication.

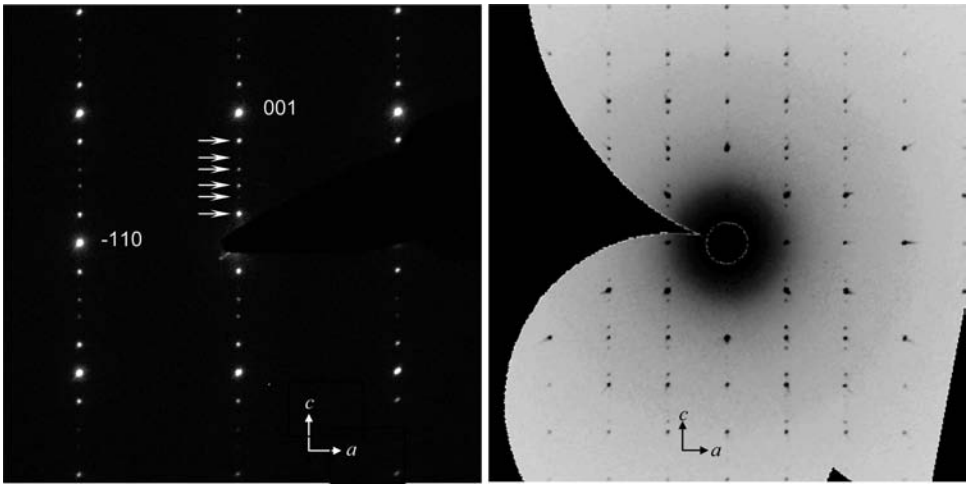

Figure 4. (Left) HRTEM of (110) plane. Incommensurately modulated peaks are marked with arrows. (Right) Reciprocal space reconstructed from X-ray diffraction data displayed along the (110) plane.

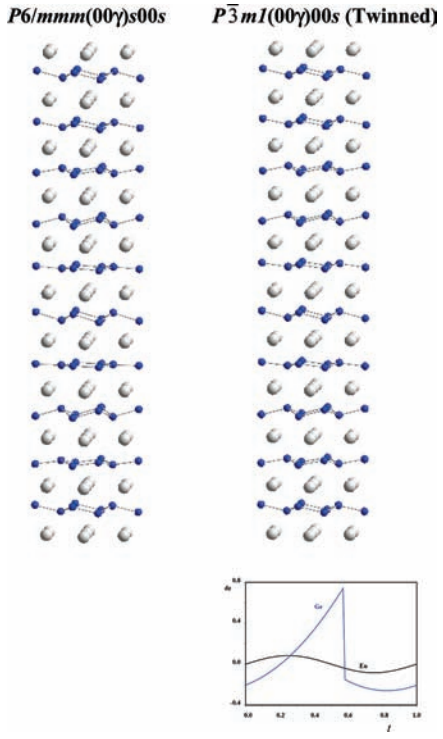

Figure 5. Incommensurately modulated structures of $Eu(Zn_{0.25}Ge_{0.75(2)})_2$ with harmonic (left) and sawtoothlike (right) modulations. Displacement along the z direction for the Eu atoms (gray curve) and Zn/Ge atoms (blue curve) as a function of the t internal coordinate.

harmonic. This modification produced a slight improvement to the fit but leads to a three-dimensional structure where the puckering of the 6^3 nets has much lower variance (0.414−0.637 Å; average value 0.549 Å) and changes orientation at regular intervals, a feature which creates resemblances to EuGaGe.[9] The distances in the 6^3 net vary from 2.485 to 2.527 Å. This second model also closely approximates an intergrowth of YPtAs-type[9] and $EuGe_2$-type[32] structures but is twinned with respect to the c axis and uses the super space group $P\bar{3}m1(00\gamma)00s$. Results of these refinements are summarized in Table 3. In Figure 5, the displacements of the Eu atoms (gray curve) and Zn/Ge atoms (blue curve) along the z direction are presented as a function of the internal coordinate t. These two curves show modulations in phase with each other, which indicates important interactions between these two subnetworks.

Regions 4 and 5: $EuGe_2$. For $x > 0.75(2)$ in $Eu(Zn_{1-x}Ge_x)_2$, the $EuGe_2$-type phase begins to appear as one of the majority phases in product mixtures, as displayed in Figure 1e. However, lattice parameters determined from powder X-ray diffraction patterns of the two-phase products do not indicate significant Zn substitution for Ge in $EuGe_2$. At $x = 1$, the $EuGe_2$-type phase (Figure 2, right) crystallizes as a single-phase, binary compound and the powder X-ray diffraction pattern is shown in Figure 1f. The $EuGe_2$-type structure is derived from the AlB_2-type structure by strong puckering of the hexagonal nets along the c axis,[31,34] but unlike $EuZn_2$, there are no Ge−Ge contacts between the 6^3 nets.

Structural Comparisons. Trends in phase behavior and crystal structures along the $Eu(Zn_{1-x}Ge_x)_2$ series can be attributed to the interplay among atomic sizes, valence electron counts, and chemical bonding types, which can be estimated by the atomic electronegativities and their differences.[35] Common AB_2 structures for A coming from the alkaline earth elements and B coming from the tetrelides (group 14), trielides (group 13), and Zn group (group 12) include the orthorhombic KHg_2 type, the trigonal $CaIn_2$ type, the hexagonal AlB_2 type, as well as the three Laves phase structure types: the cubic $MgCu_2$ type and the hexagonal $MgZn_2$ and $MgNi_2$ types. A recent analysis of six-electron and eight-electron AB_2 phases indicates that AlB_2-type structures are preferred for large size ratios (V_A/V_B) and electronegativity differences ($\chi_B - \chi_A$), whereas the KHg_2-type structure becomes preferred as the corresponding electronegativity difference becomes smaller while the size ratio remains constant.[36] Laves phase structures dominate when these two parameters are smaller, which has been

(34) Pöttgen, R. *J. Alloys Compd.* **1996**, *243*, L1.
(35) Hoffmann, R.; Pöttgen, R. *Z. Kristallogr.* **2001**, *216*, 127.
(36) Amerioun, S. *Phase and Structural Stability Principles of Polar Intermetallic AeE_4 and AeE_2 Systems (Ae = Ca, Sr, Br; E = Al, Ga, In)*; Ph.D. thesis, Stockholm University, Stockholm, Sweden, **2003**.

Table 3. Crystallographic Data for $Eu(Zn_{0.25}Ge_{0.75(2)})_2$

crystal system	trigonal
super space group	$P\bar{3}m1(00\gamma)00s$
γ ($q = \gamma c^*$)	0.2200(1)
cell parameters (from 1027 reflections centered on 1612)	
a_s (Å)	4.2349(13)
c_s (Å)	4.5891(14)
V_s (Å^3)	71.28(1)
obsd. data/params	222/12
R overall indices [$I > 3\sigma(I)$]	R = 6.33%, GOF = 2.81
R_0 main refln	R = 5.38%/128 reflns
R_1 sat. first-order refln	R = 9.72%/94 reflns
twin ratio	0.485(10)

Occupational Waves (Legendre Polynomials)

Ge	Δ	1
	$S_{\Delta,1}$	0.178(8)
	$C_{\Delta,1}$	0

Positional Parameters ($u(\bar{x}_4) = \sum_{n=1}^{k} S_n \sin(2\pi n\bar{x}_4) + \sum_{n=1}^{4} C_n \cos(2\pi n\bar{x}_4)$)

atom	harmonic coeff.	x	y	z	U_{eq}
Eu		0	0	0	0.0139(4)
	$S_{x3,1}$			0.0182(8)	
	$C_{x3,1}$			0	
Ge		1/3	2/3	0.4889(14)	0.0226(11)
	$S_{x3,1}$		0	0.096(3)	
	$C_{x3,1}$			0.066(5)	

ADP Harmonic Parameters

atom	U_{11}	U_{22}	U_{33}	U_{12}	U_{13}	U_{23}
Eu	0.0128(4)	0.0128(4)	0.0162(6)	0.0064(2)	0	0
Ge	0.0119(6)	0.0119(6)	0.044(3)	0.0059(3)	0	0

interpreted as effective packing of differently sized metal atoms.[37] The 12-coordinate metallic radius of Eu is 2.04 Å, which lies between that of Sr and Ba, and Eu is slightly more electronegative than these elements according to Pauling's scale. For the $Eu(Zn_{1-x}Ge_x)_2$ series, there is a large size ratio ($V_{Eu}/V_{Zn/Ge}$) and an increasing electronegativity difference ($\chi_{Zn/Ge} - \chi_{Eu}$) as the Ge content increases, which implies a switch from orthorhombic KHg_2-type to hexagonal AlB_2-type phases as the valence electron count varies from six ($EuZn_2$) to eight electrons (EuZnGe). Of particular interest is the incommensurate modulation occurring for the nine-electron case ($EuZn_{0.5}Ge_{1.5}$), modulations which resemble structural behavior in other nine-electron examples, for example, CaAlSi[38] and numerous AeTrTt (BaGaGe; Ae = alkaline-earth metal; Tr = trielide metal; Tt = tetrelide element).[39]

The observed structural transformations along the $Eu(Zn_{1-x}Ge_x)_2$ series can be illustrated using the *Bärnighausen* tree[40,41] of group−subgroup relationships. As shown in Figure 6, the KHg_2-type structure derives from the ortho-hexagonal setting of the AlB_2-type structure (space group $C2/m2/m2/m = Cmmm$) via a *translationengleiche* transformation of index 3 ($t3$), followed by a *klassengleiche* transformation of index 2 ($k2$) to space group $I2_1/m2_1/m2_1/a = Imma$. On the other hand, the trigonal $EuGe_2$-type structure arises by puckering of the hexagonal nets of the AlB_2-type structure. This symmetry reduction from AlB_2 to $EuGe_2$ occurs via a *translationengleiche* transformation of index 2 ($t2$) of $P6/m2/m2/m$ ($P6/mmm$) to space group $P\bar{3}m1$.[35]

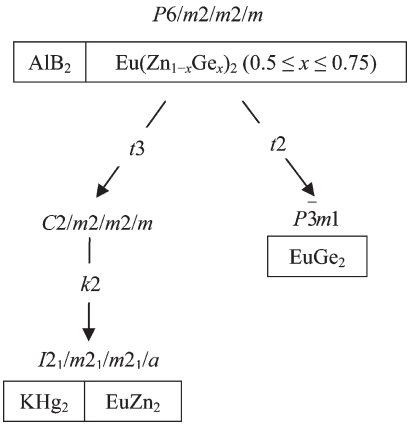

Figure 6. The *Bärnighausen* tree of group−subgroup relationships of the AlB_2 derivatives for KHg_2-type and $EuGe_2$-type structures.

A final structural consideration of the $Eu(Zn_{1-x}Ge_x)_2$ series is the monotonic increase of the $(c/a)^*$ ratios and unit cell volumes, which are listed in Table 1, as the Ge content (x) increases, while the 6^3 nets vary from puckered in $EuZn_2$ to planar in $EuZn_{1-y}Ge_{1+y}$, and then to puckered in $EuGe_2$. The trend in unit cell volumes counters expectations based on the relative sizes of Zn and Ge, whether 12-coordinate metallic or covalent radii are used. However, the increasing $(c/a)^*$ ratios suggest an increasing repulsion between adjacent $^2_\infty[(Zn_{1-x}Ge_{1+y})_2]$ 6^3 nets. The relationship between the puckering of the 6^3 nets and the $(c/a)^*$ ratios also depends on the electronic structure.[8] At low $(c/a)^*$ ratios, puckering is driven by an increasing occupation of intraplane π-antibonding orbitals through interplane p−p σ overlap. As the $(c/a)^*$ ratio increases, this σ overlap steadily decreases, and the 6^3 network becomes planar, as in graphite. The puckering observed in $Eu(Zn_{0.25}Ge_{0.75(2)})_2$ and $EuGe_2$, however, can be attributed to the local electronic structure at Ge, which can be rationalized by the Zintl−Klemm concept. All of these intriguing features will be addressed by analysis of electronic structure calculations in the companion paper.[29]

The Zintl−Klemm Concept. At the Ge-rich end of the $Eu(Zn_{1-x}Ge_x)_2$ series, that is, $EuGe_2$, the puckered, three-bonded $^2_\infty[Ge_2]$ net follows from the Zintl−Klemm formalism for $[Ge_2]^{2-}$, which is based on divalent Eu atoms. The five-electron Ge^-, which is isoelectronic with As, prefers trigonal-pyramidal coordination by using its valence electrons to form three two-center, two-electron σ bonds and one lone pair. Implicit in this interpretation is an ionic formulation that follows the relative electronegativities: on the Pauling scale, $\chi(Eu) = 1.2$ and $\chi(Ge) = 2.01$. On the other hand, $EuZn_2$ is electron-deficient and does not satisfy the Zintl−Klemm formalism: the 4b-3D network of Zn atoms would require four valence electrons

(37) Johnston, R. L.; Hoffmann, R. *Z. Anorg. Allg. Chem.* **1992**, *616*, 105.
(38) Sparta, K. M.; Müller, R.; Merz, M.; Roth, G.; Adelmann, P.; Wolf, T. *Acta Crystallogr.* **2006**, *B62*, 710.
(39) Häussermann, U. Private communication.
(40) Bärnighausen, H. *Common. Math. Chem.* **1989**, *9*, 139.
(41) Bärnighausen, H.; Müller, U. *Symmetriebeziehungen zwischen den Raumgruppen als Hilfsmittel zur straffen Darstellung von Strukturzusammenhängen in der Kristallchemie*; Universität Karlsruhe and Universität-Gh Kassel: Germany, 1996.

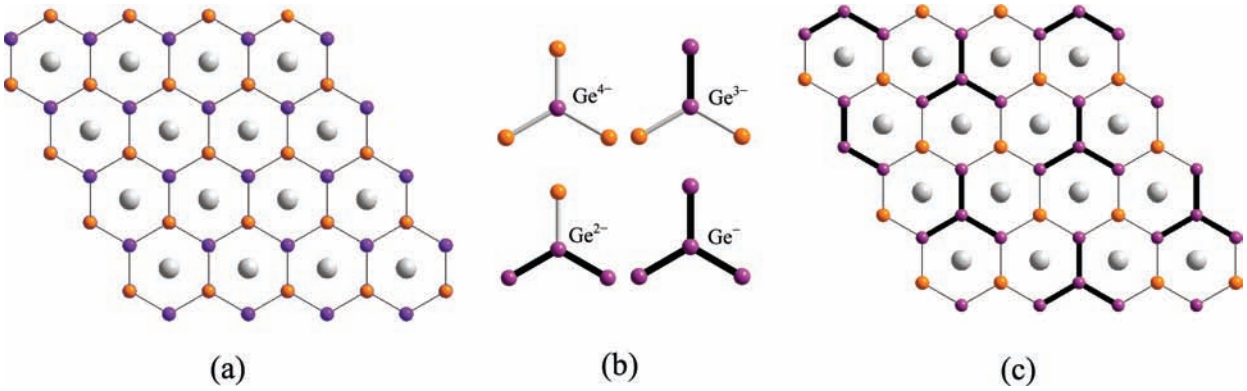

Figure 7. (a) Alternant 6^3 net of [ZnGe]. (b) The four different local coordination environments at Ge. (c) The layer with [Ge_4] stars. Eu, gray; Zn, orange; Ge, purple.

per Zn atom. Nevertheless, Zn is more electronegative than Eu (χ(Zn) = 1.66), and the formal oxidation state of Zn is −1 in $EuZn_2$, a state which assigns three valence electrons per Zn atom. Therefore, at some point along the $Eu(Zn_{1-x}Ge_x)_2$ series, the Zintl−Klemm formalism, which relates local electronic structure and chemical bonding features, must change validity.

According to our results, this point occurs at Eu $(Zn_{0.50}Ge_{0.50})_2$ = EuZnGe. For ternary Eu−Zn−Ge phases, the relative electronegativities suggest that Ge will attract electrons more strongly than Zn atoms. Thus, as Ge atoms replace Zn atoms in $Eu(Zn_{1-x}Ge_x)_2$, the formal oxidation state of Zn will rapidly increase from −1 in $EuZn_2$ toward +2 in EuZnGe, as long as there are no short Ge−Ge contacts. In light of our experimental results that the minimum Ge content for AlB_2-type single phases is $EuZn_{1.00}Ge_{1.00(2)}$, we can formulate this limiting composition as the closed-shell compound Eu^{2+}-$Zn^{2+}Ge^{4-}$. According to the Zintl−Klemm formalism, there will be no short Ge−Ge contacts within the planar 6^3 nets, so the only solution is an alternant $^2_\infty[ZnGe]^{2-}$ net (see Figure 7a). As a corollary, there will be no short Zn−Zn contacts. Since X-ray diffraction could not distinguish Zn and Ge atoms, a completely random distribution of these two atoms does allow for homonuclear contacts, which will violate the Zintl−Klemm rules. Thus, we assume that each 6^3 net in $EuZn_{1.00(2)}Ge_{1.00(2)}$ is an alternant $^2_\infty[ZnGe]^{2-}$ net but that they stack randomly along the *c* axis. Furthermore, we express those $Eu(Zn_{1-x}$-$Ge_x)_2$ phases for which the Zintl−Klemm formalism holds as $EuZn_{1-y}Ge_{1+y}$, for which $0 \le y \le 1$.

The Zintl−Klemm concept provides a relationship between the average formal charge and the average coordination for main group elements in a chemical structure based on the octet rule.[2−4] In $EuZn_{1-y}Ge_{1+y}$, if we treat Eu and Zn as each donating two valence electrons to Ge, then the following relations hold:

$$\text{average formal charge per Ge atom} = -\frac{4-2y}{1+y}$$

$$\text{average valence electron count per Ge atom} = 4 + \frac{4-2y}{1+y} = \frac{8+2y}{1+y}$$

and

$$\text{average Ge−Ge connectivity} = 8 - \frac{8+2y}{1+y} = \frac{6y}{1+y}.$$

These relationships are plotted in Figure 7. Therefore, for the $EuZn_{1-y}Ge_{1+y}$ series, the average formal charge at Ge can vary from −4 (EuZnGe) to −1 ($EuGe_2$), while the average number of Ge−Ge bonds per Ge atom change from 0 (EuZnGe) to 3 ($EuGe_2$). Integral formal charges at Ge also occur for $EuZn_{0.8}Ge_{1.2}$ (−3; one-bonded Ge) and $EuZn_{0.5}Ge_{1.5}$ (−2; two-bonded Ge). For a given chemical formula, however, there can be numerous structural solutions that will satisfy these predictions.

According to our experimental results, the $EuZn_{1-y}$-Ge_{1+y} series adopts an AlB_2-type structure. Therefore, the Zintl−Klemm formalism should also be compatible with the structural constraints. In this regard, there are numerous potential solutions. We explore two specific cases here.

1. Random *Distribution* of Zn and Ge Atoms in Each 6^3 Net. In this model, the occupation of each atomic site of the honeycomb net is determined by the composition. The fraction of Zn atoms is $(1 - y)/2$; the fraction of Ge atoms is $(1 + y)/2$. Surrounding a Ge site, there will be a binomial distribution of (3 Zn), (2 Zn + 1 Ge), (1 Zn + 2 Ge), and (3 Ge) coordination environments (shown in Figure 7b); each of these four concentrations are plotted as a function of *y* in Figure 8. If we use the Zintl−Klemm formalism for this random distribution and compare the average Ge valence electron count and Ge−Ge connectivity, there are significant deviations at low *y* values from the behavior anticipated by the equations above, which are derived just from the chemical formula. Specifically, for $y = 0$, that is, EuZnGe, the random distribution of Zn and Ge atoms would predict an average formal charge at Ge of −2.5, which implies an average 1.5-bonded Ge atom. This evaluation of the local electronic structure at Ge, as well as Zn, contradicts expectations from electronegativity arguments.

(2). Random *Replacement* of Zn by Ge on the Alternant 6^3 Net. In this case, we start from the alternant $^2_\infty[ZnGe]^{2-}$ net anticipated for EuZnGe and replace Zn with Ge atoms. This model guarantees keeping the Zn atoms widely separated so that there are no close Zn−Zn contacts. Furthermore, as the Ge content increases, the connectivity of Ge atoms steadily increases. At low

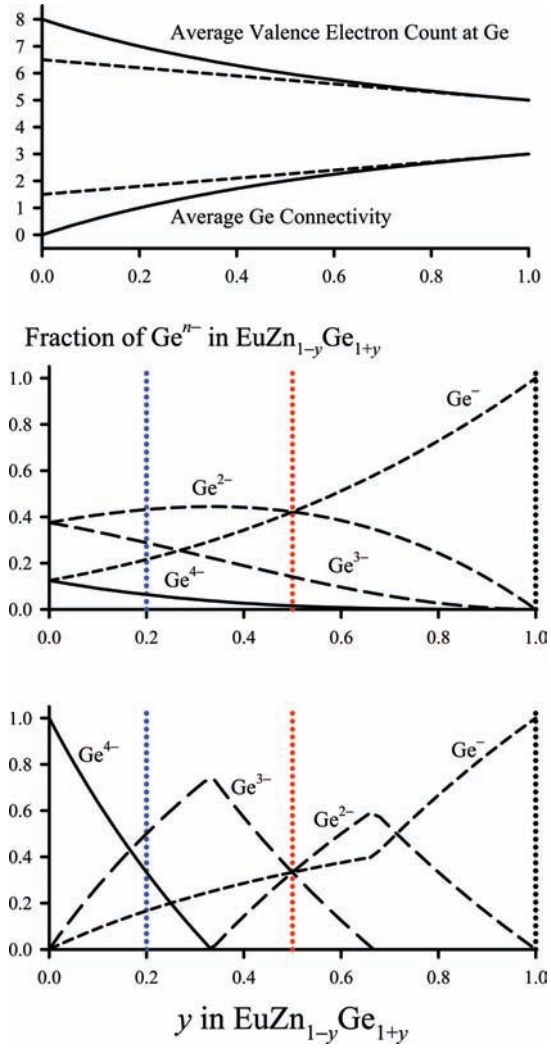

Figure 8. (Top) Average connectivity and valence electron count in $EuZn_{1-y}Ge_{1+y}$ for random and alternant 6^3 net. (Bottom) Concentrations of different Ge sites in random (middle) and alternant (bottom) nets in $EuZn_{1-y}Ge_{1+y}$.

concentrations, trigonal Ge_4 stars emerge. For these fragments to remain planar, we expect their formal charge to be −8: $[Ge_4]^{8-}$ would be isoelectronic to the planar CO_3^{2-} ion, and there are numerous examples of these Zintl ions.[42] On the other hand, simply from the Ge−Ge connectivity, the formal charge can be −10, but we would expect the central Ge atom to adopt a pyramidal local coordination because $[Ge_4]^{10-}$ is isoelectronic with SO_3^{2-}. If we keep the Zn atoms most widely separated, Ge atoms will belong only to such Ge_4 stars in the limiting case, $Eu_3Zn_2Ge_4 = EuZn_{0.67}Ge_{1.33}$, which is illustrated in Figure 7c. Further replacement of the Zn atoms by Ge atoms creates larger Ge-based fragments that can grow continuously until $EuGe_2$ is achieved.

Thus, the Zintl−Klemm formalism provides a rationale for the Zn-rich end of the AlB_2-type $EuZn_{1-y}Ge_{1+y}$ phases, that is, low y values, but does not explain our experimental results at the Ge-rich end. Nevertheless, this electron counting rule eliminates a completely random distribution of Zn and Ge atoms within each 6^3 net as a viable solution that is compatible with both local geometrical structure and local electronic structure. Furthermore, a drastic change in the formal oxidation state of Zn occurs in the Zn-rich region of the entire $Eu(Zn_{1-x}Ge_x)_2$ series. Therefore, electronic structure theory is essential to providing an understanding of the relationship between chemical structure and electronic structure in these $Eu(Zn_{1-x}Ge_x)_2$ phases, a theory which is the subject of the accompanying paper.[29]

Summary

A total of 15 different compositions in the $Eu(Zn_{1-x}Ge_x)_2$ series ($0 \le x \le 1$) were prepared using induction melting and characterized by powder and single-crystal X-ray diffraction to study the influence of valence electron count on structural trends. As the Ge content increases, the $Eu(Zn_{1-x}Ge_x)_2$ series varies from the orthorhombic KHg_2 type to the hexagonal AlB_2 type, and finally to the trigonal $EuGe_2$ type, with two-phase regions between each of these three single-phase regions. $EuZn_2$ allows restricted substitution of Zn by Ge atoms, whereas there is no observable Zn replacement for Ge in $EuGe_2$. The hexagonal AlB_2-type phases occur for a range of compositions from $EuZn_{1.00}Ge_{1.00(2)}$ to ca. $EuZn_{0.50}Ge_{1.50(2)}$. Although structure solutions yield planar $^2_\infty[(Zn_{1-x}Ge_x)_2]$ 6^3 nets, the U_{33}/U_{11} ratios suggest increasing pyramidalization of these nets as the Ge content increases. Although these single-crystal X-ray diffraction results could not distinguish Zn and Ge atoms, subsequent theoretical calculations indicate alternant [ZnGe] nets in EuZnGe and continued Zn segregation in these $EuZn_{1-y}Ge_{1+y}$.[29] The $9e^-$ $EuZn_{0.50}Ge_{1.50(2)}$ exhibited incommensurate modulation along the c direction, a structural feature that has been seen in other $9e^-$ AlB_2-type phases[38,39] and could be resolved by a super space group approach. The resulting structural model showed puckering of the 6^3 nets in modes similar to both $EuGe_2$[32] and EuGaGe (YPtAs-type).[9]

Furthermore, the AlB_2-type phases show increasing separation between the 6^3 nets and unit cell volumes with increasing Ge content, which contrasts with the atomic size relationship between Zn and Ge. Magnetic susceptibility and temperature-dependent electrical resistivities indicate divalent Eu behavior as well as semiconducting or semimetallic characteristics. Therefore, the Zintl−Klemm electron counting rule is an attractive formalism to account for the possible structural and physical behavior of these AlB_2-type phases. However, the Zintl−Klemm formalism accounts for just one end of the AlB_2-phases, that is, $EuZn_{1.00}Ge_{1.00(2)}$, but does not explain the upper bound in Ge content at $EuZn_{0.50(2)}Ge_{1.50(2)}$. To accomplish this, as well as to understand the structural and bonding features of the entire $Eu(Zn_{1-x}Ge_x)_2$ series, theoretical electronic structure calculations are imperative and have been conducted and analyzed.[29]

Acknowledgment. This work was supported by NSF DMR 02-41092 and 06-05949. The authors are grateful to Dr. Warren Straszheim at Iowa State University for the EDXS measurements and to Dr. Walter Schnelle at Max-Planck-Institute for Chemical Physics of Solids in Dresden, Germany, for magnetization measurements. We would also like to thank Dr. Vaclav Petricek for his helpful contributions on the super space group approach.

(42) Eisenmann, B.; Klein, J.; Somer, M. *Angew. Chem., Int. Ed. Engl.* **1990**, *29*, 87.

To show that first-order harmonic modulations at the origin (Eu sites) are not allowed in the super space group $P6/mmm(00\gamma)s00s$, we show the effect of the two symmetry operations, emphasized in boldface as $\boldsymbol{P6}/mmm(00\gamma)\boldsymbol{s}00s$ and $P6/mm\boldsymbol{m}(00\gamma)s00\boldsymbol{s}$, on the first-order harmonic of the $x3$ coordinate, i.e., the z-coordinate. The two symmetry operations are $(x1\ x2\ x3\ x4) \rightarrow (x1-x2\ x1\ x3\ x4 + 1/2)$ and $(x1\ x2\ x3\ x4) \rightarrow (x1\ x3\ x2\ x4 + 1/2)$. For the Eu atoms at the origin, (0 0 0), both symmetry operations perform the following transformation: $(0\ 0\ 0\ x4) \rightarrow (0\ 0\ 0\ x4 + 1/2)$. The first harmonic along the z-direction is $U_{x3,1}(\nu) = S_{x3,1}\sin(2\pi\nu) + C_{x3,1}\sin(2\pi\nu)$, where ν is the internal coordinate, and $S_{x3,1}$, $C_{x3,1}$ are the refinable first-order coefficients of the harmonic expansion of the modulation. These symmetry operations imply that $U_{x3,1}(x4) = U_{x3,1}(x4 + 1/2)$, which is true if and only if $S_{x3,1}$ and $C_{x3,1}$ are 0. Therefore, first-order harmonics would be disallowed.

Supporting Information Available: X-ray crystallographic files in CIF format, lattice constants and anisotropic displacement parameters from single-crystal diffraction, comparison of two super space group refinements of $Eu(Zn_{0.25}Ge_{0.75(2)})_2$, and temperature-dependent electrical resistivities of $Eu(Zn_{0.45}Ge_{0.55(2)})_2$ and $Eu(Zn_{0.33}Ge_{0.67(2)})_2$, and temperature-dependent magnetic susceptibilities of $Eu(Zn_{0.48}Ge_{0.52(2)})_2$ and $Eu(Zn_{0.30}Ge_{0.70(2)})_2$. This material is available free of charge via the Internet at http://pubs.acs.org.